International Forum on Aeroelasticity and Structural Dynamics
IFASD 2019
9-13 June 2019, Savannah, Georgia, USA

LOW-COST WIND TUNNEL STUDIES OF GUST ALLEVIATION CONTROL TECHNIQUES

**B. Barzgaran, J. Quenzer, A. Zongolowicz, K. Hinson,
M. Mesbahi, K. Morgansen, E. Livne**[1]

[1]University of Washington
Seattle, WA, 98195, USA
{barzb, jakeq, ajzongo, khinson}@uw.edu
{mesbahi, morgansen, eli}@aa.washington.edu

Keywords: structural dynamics, aeroelasticity, optimal control, wind tunnel experiments

Abstract: A low-cost gust load alleviation wind tunnel testing capability has been developed for the University of Washington's 3ft by 3ft low-speed wind tunnel. The two main components of the resulting system are a flexible half span wind tunnel model and a gust generation system. The wind tunnel model is an actively-controlled flexible wing / fuselage / tail configuration. In addition to presenting the system, the paper presents initial gust load alleviation results using Model Predictive Control. The system is versatile by design and allows testing of a wide range of configurations and an extensive selection of control laws at low costs.

1 INTRODUCTION

The potential for significant airframe structural weight reductions made possible by active control technology has been recognized for many years. Since gust loads can be critical in sizing large sections of an aircraft, Gust Load Alleviation (GLA) systems have become an important part of modern, highly optimized, flexible aircraft systems [1]. In a continuous effort to develop the technology, many alternative approaches to the synthesis of control laws for GLA have been studied to date. Control law synthesis and implementation for GLA are still active areas of research and development with numerous papers and reports on the subject every year.

The aircraft systems to be optimized and controlled are multidisciplinary, complex, and uncertain. They operate over a large range of flight conditions. Hardware limitations present constant challenges. Mathematical models still cannot capture the physical behavior well enough, especially in the early stages of design when experimental results are not yet available [2]. Wind tunnel tests have always been, therefore, very important for the development of the technology. In the past, limitations on miniature hardware elements such as actuators and sensors plus the high costs of testing in large wind tunnels (government owned or commercial) limited the testing of GLA systems to major development projects.

The revolution in miniaturization of control systems hardware over the last 20 years has led to a growing number of investments by research organizations in low-cost aeroelastic wind tunnel testing capabilities. These low-cost wind tunnels allow for cost effective, rapid wind tunnel tests of aeroelastic active control technology, validating and testing the limits of model-based control system designs. References [3] - [22] in the bibliography present a selection of publications on wind tunnel gust generation systems in large and small wind tunnels that are the basis of active control wind tunnel testing capabilities of the organizations involved.

Figure 1: Test article installation in the wind tunnel.

The University of Washington's William E. Boeing Department of Aeronautics and Astronautics operates two low speed wind tunnels. A modern 3ft by 3ft low-speed tunnel housed in the historic 1917 wind tunnel building built at the university with funds by the young Boeing company, and the Kirsten Wind Tunnel, a commercial low-speed tunnel with a 12 ft x 8 ft test section completed in 1939. With the goal of adding experimental capabilities to our work in the area of aeroservoelastic active control, Gust Generation Systems (GGS) have been developed for both tunnels.

The paper will briefly present the GGS built for the 3x3 wind tunnel. It will proceed to discuss exploratory GLA studies, simulation-based and experimental, that are part of research at the University of Washington focused on the GLA of modern flexible aircraft.

One of the simulation systems developed as part of the aeroservoelastic simulation and control synthesis capability has been described in a prior publication [23]. Another paper, [24], describes the development of a low-cost wing / fuselage / tail active aeroservoelastic test article for GLA testing of different control law synthesis methods.

The aeroservoelastic wind tunnel test article is presented first in Section 2. The design, fabrication, and validation of the Gust Generation System is discussed in Section 3. Section 4 briefly presents basic Model Predictive Control (MPC) theory and shows initial closed-loop optimal control results for GLA. The conclusion Section 5 summarizes the results and presents plans for future work.

2 AEROSERVOELASTIC WIND TUNNEL TEST ARTICLE

The development of the aeroservoelastic wind tunnel test article for studying the performance of GLA control laws in the 3x3 tunnel is detailed in [24] and summarized here. The design of the test article was driven by two factors: the need to capture in testing aeroelastically coupled rigid-body and elastic motions and the physical constraints of the test facility. A half-span wing / fuselage / tail configuration was selected, see Figure 1. The vehicle mounts to the ceiling of the wind tunnel, positioned so that the wing tip points downwards, see Figure 2. Structurally the vehicle consists of three beams, one for each of the fuselage, wing, and tail components. Aerodynamically, the wing and tail use NACA-0012 airfoils. The aerodynamic shells used to create the aerodynamic shape (outer mold line) of the lifting surfaces have a chordwise slot through which the structural beam - a thin metal strip - passes. The wing consists of five aerodynamic shells with foam between them spanwise to minimize aerodynamic shell effects on stiffness as determined by the beam structure. This construction technique is very common in the design of low-speed aeroelastic scaled models [25]. The tail consists of one aerodynamic shell since tail bending was not important in the GLA tests for which this first aeroservoelastic model was developed. There is a concentrated mass at the wing tip. The vehicle is mounted at the wing's quarter chord and is free to rotate about the wing's pitch axis.

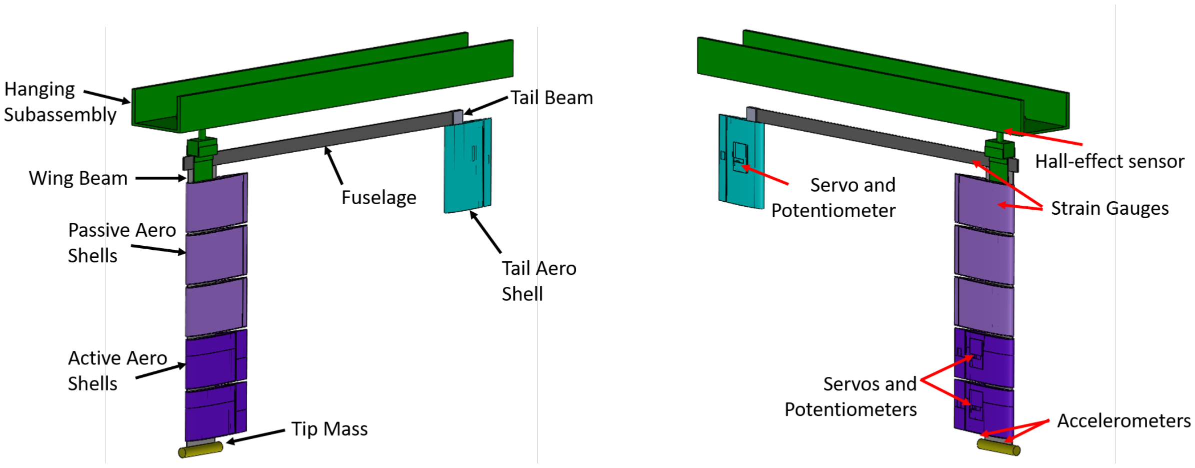

(a) Primary model components

(b) Sensing and actuation components

Figure 2: Principal components of the first test article.

A secondary objective was that the construction of the vehicle would make configuration modifications simple and low-cost. As examples, the aerodynamic shells on the wing are interchangeable and may be active (contain a servo motor and control surface) or inactive. The model can be tested with five active wing aerodynamic strips or only one or none. The wing-tip mass can be more concentrated or elongated in the form of a long aerodynamic tip-tank with a center of mass that can be moved forward or aft along the tip chord of the wing. The beam representing the fuselage can be replaced to yield different fuselage stiffness characteristics. Details of the structural configuration are provided in Table 1.

Component	Material
Wing Beam	Aluminum 6061-T6
Tip Cyliner	Brass
Aero-shell	Polylactic Acid (PLA)
Fuslage Beam	Low Carbon Steel
Tail Beam	Aluminum 6061-T6

(a) Materials

Component	Weight (lb)
Wing Beam	0.367
Tip Cylinder	0.276
Active Aero-shell	0.209
Passive Aero-shell	0.132
Fuselage Beam	0.986
Tail Beam	0.146

(b) Masses

Table 1: Overview of structural components.

The particular test article discussed in this paper is configured with two aileron control surfaces (on the wing's two outer aerodynamic shells) and a single full-span elevator surface. Each surface is driven by an MKS HV6130 servo motor embedded inside the aero-shell.

Seven on-board sensors measure the following parameters (Figure 2): Pitch angle, forward and aft wing tip acceleration, wing root strain, inboard and outboard aileron deflection, and elevator deflection.

The rigid-body pitch angle is measured by a Hall effect sensor. This sensor is a non-contact sensor which employs two components: a magnet attached to the test article and a device to measure rotation of the associated magnetic field. The benefit of a non-contact sensor is that it does not add damping to the pitch degree of freedom. Wing tip accelerometers are mounted at the forward and aft corners of the wing beam. The vehicle is constrained from rigid-body plunge translation. The accelerations measured at the wing tip are used to measure the wing's bending and torsional motions. A strain gauge is attached at the wing root for a direct measurement of root bending strain. The accelerometers and strain gauge are complimentary in sensing the structural state of the wing (which is of interest in GLA control law design). Finally, rotary potentiometers are installed on the output shaft of each of the control surface servo motors and provide measurements of control surface position.

The Simulink Desktop Real-Time application is used to coordinate sensor measurements and control commands for active control of the test article in the wind tunnel. A flow chart of the closed loop control process is shown in Figure 3.

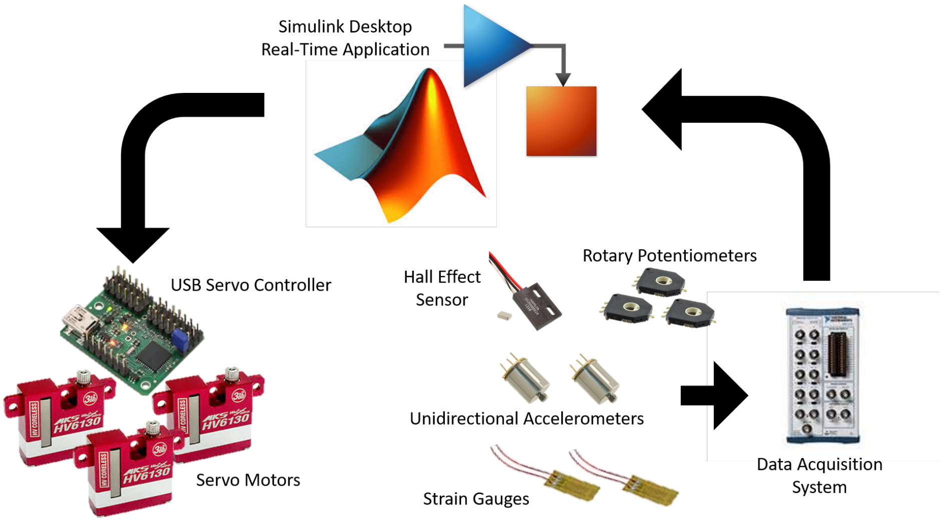

Figure 3: Signal flow in the experimental configuration of the real-time control software.

2.1 Analytical / Numerical Modelling

A mathematical model of the test article is needed for development of control algorithms as well as for safety analysis of the unaugmented system (flutter, divergence). The modelling approach used in the first steps of the development described here originated in the 1960s [26] and is well documented in flight dynamics and control textbooks [27, 28]. The method utilizes the mean-axis approach to the structural dynamics of a deformable body. It is assumed that there are small structural deflections, small angles of aerodynamic incidence, and small changes in mass or inertia. Following the process described in [23], a linear time-invariant state space representation is generated using quasi-steady aerodynamics with a a NASTRAN finite element model of the test article. Such a model has the form

$$\dot{x}(t) = Ax(t) + Bu(t), \tag{1}$$

where $x \in \mathbb{R}^n$ is the time depended state vector, $u \in \mathbb{R}^m$ is the control vector, and the matrices A and B are state and control matrices, respectively. The state vector has the following elements ($n = 6$): angle or attack, pitch rate, and four modal generalized coordinates representing the first two structural modes. Modal generalized displacements are used to approximate structural elastic deflection (q) in terms of a specific reduced order basis,

$$q \approx \Phi\eta, \tag{2}$$

where Φ is a matrix of normal modes, and η is the vector of modal generalized displacements. The dynamic effects are partitioned as:

$$A = \begin{bmatrix} A_r & A_{re} \\ A_{er} & A_e \end{bmatrix}, \tag{3}$$

where the matrix $A_r \in \mathbb{R}^{2\times2}$ represents the linearized rigid body dynamics and aerodynamic coefficients, matrix $A_{re} \in \mathbb{R}^{2\times4}$ contains the aerodynamic forces and torques that result from structural motion, matrix $A_{er} \in \mathbb{R}^{4\times2}$ contains the forces and torques imparted upon the structure due to rigid body motion, and matrix $A_e \in \mathbb{R}^{4\times4}$ represents the linear structural dynamics (where each mode shape behaves as a second order system).

3 GUST GENERATION SYSTEM DEVELOPMENT

Various alternative configurations for a gust generating multi-vane system were considered. In such systems a set of vanes at the entrance of the test section, ahead of the wind tunnel model, is motion-controlled to produce gusts of desired shape and duration. The vanes have to span the height (or width) of the test section. Vanes too close to the floor and ceiling (or side walls) are usually not as effective. An effort was made to space the vanes so that the wind tunnel model would not be in their wakes. A few additional considerations have to be taken into account. First, large vanes (with a large chord) may produce stronger gusts but may be slow to respond to command inputs because of high inertia. The vanes have to be stiff, with natural frequencies that are well above the frequency range of interest and with minimal distortion of the desired uniform gusts for the tests planned. And, finally, the vanes should not stall in the range of operation that would produce gusts of required magnitude on the wind tunnel model. Because of the very tight schedule and low cost engineering analysis studies of the GGS were limited to quick estimates based on aerodynamic potential theory, some steady CFD based models, and reported results by the developers of similar systems for other wind tunnels, especially [5], [16], and [19].

The configuration selected is based on two vanes of NACA 0012 airfoil shapes with 10 inch chords. The vanes are placed vertically at the entrance to the 3ft by 3ft test section, placed 7 inch each from the center line of the test section. The natural frequencies of the vanes are above 20 Hz. To allow quick installation and removal of the vanes, an extension insert was developed for the wind tunnel ahead of its test section. It is designed for the installation of various excitation and measurement systems. The system is shown in Figure 4 .

The full GGS, which encompasses the wind tunnel extension with mounting plates (visible in Figure 4 (b)), the gust vanes, and the software control system, was designed and constructed to University of Washington specifications by Aeronautical Testing Service Inc., of Arlington, Washington. The system is accessed via an http-protocol through a local network, where gusts with pre-defined wave forms are generated, initiated by manual command. The commanded gusts are driven by a motor controller connected to the gust vanes via an external motor.

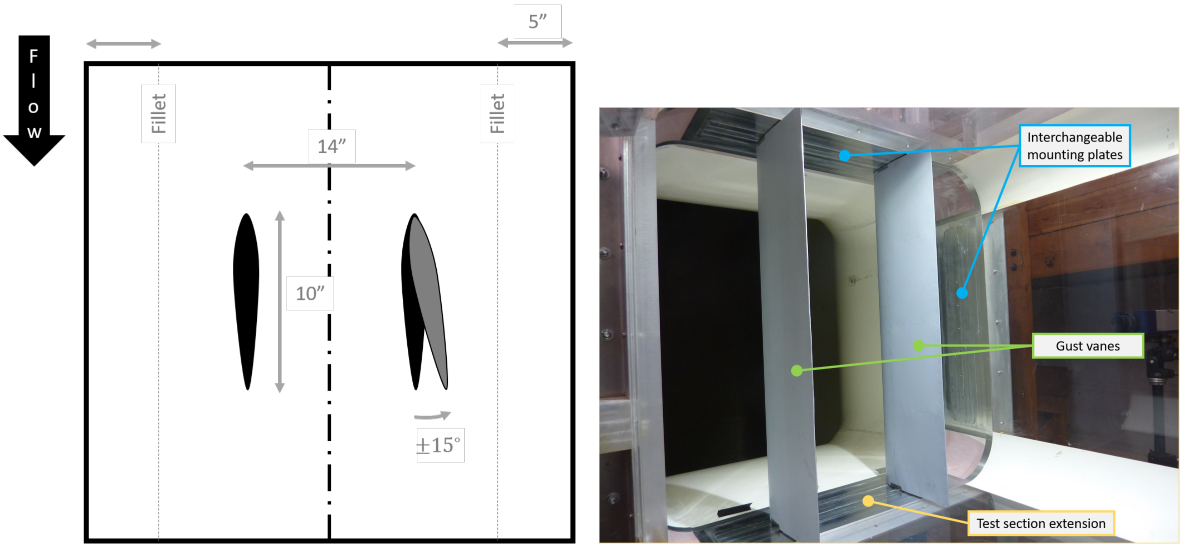

(a) Schematic gust vane configuration (b) Installed gust vanes

Figure 4: Specification and installation of the gust generation system.

3.1 Gust System Validation

After initial installation of the GGS in the 3x3 tunnel, its shakedown and validation were done in two phases. The system was studied first in steady state conditions, with the vanes set to certain fixed angles relative to the incoming flow. This study was followed by dynamic tests. The following paragraphs describe the shakedown of the GGS.

The first step in the shakedown phase was to set the vanes at a static angle of attack and to increment the tunnel wind speed to check for changes in structural vibration or deformation of the vanes. In Figure 5, the thin blue line is the acrylic wall of the wind tunnel test section. A laser vibrometer, outside of the tunnel, is pointed at a mid-span point on the gust vane to measure changes in vane position. The vane shown is the right-hand vane looking in from the top of the wind tunnel.

Figure 6 provides the measurements taken from that first round of tests. For each colored dataset (each corresponding to a “fixed” nominal angular vane displacement), the tunnel started at zero wind speed and the wind was subsequently increased by hand through four target velocities. The first four angular positions demonstrate qualitatively similar behavior wherein increased velocity generated a corresponding increase in trailing edge displacement. The vanes clearly rotate from their initial angles due to aerodynamic load. These rotations, however, are very small.

The positive values of displacement in this figure correspond to the trailing edge getting closer to the laser. The laser was zeroed at each new initial angular setting of the vanes, so the measurements of Figure 6 depict deviations from the wind-off position of the vane. The rather dramatic difference in behavior between initial angle of attack of 10° and initial angle of attack 12° led to a follow-on test with new test points to determine if the unique behavior at 12° was repeatable and if the transition to that behavior was sudden or gradual.

The follow-on test data are shown in Figure 7 which provides the following insights: the notably different response at an initial angle of 12° is both repeatable and sudden. Note that increasing moment due to aerodynamic pitching moment and spanwise bending due to lift should both act

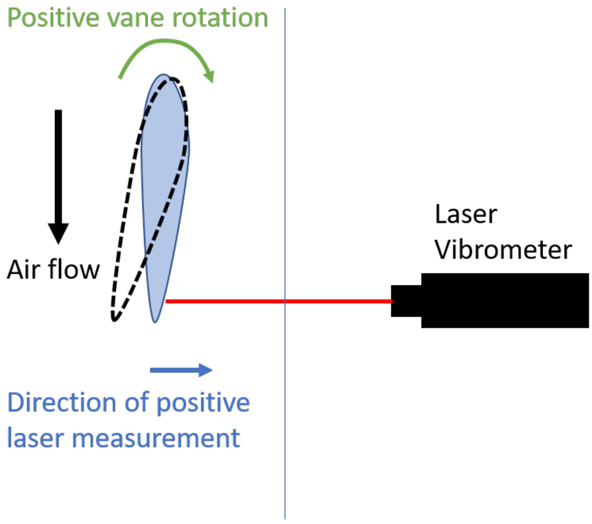

Figure 5: Vane-laser measurement configuration used in evaluating aeroelastic behavior of the gust generation vanes.

to displace the trailing edge closer to the laser (increase the laser displacement measurement). Thus, it is not clear from the figures shown so far if the increases in trailing edge displacement are primarily due to spanwise bending or rigid body rotation of the vanes. Moving the laser to a point near one of the hinges of the vane (as far away from the center of its span as possible) would tell us whether vane rotation or vane bending are the deciding factors or some combination of them. However, since the measured trailing edge displacements were very small in terms of their effect on actual vane angle of attack at its mid span and because of the tight development schedule, such studies were not deemed necessary before proceeding to the first series of GLA tests.

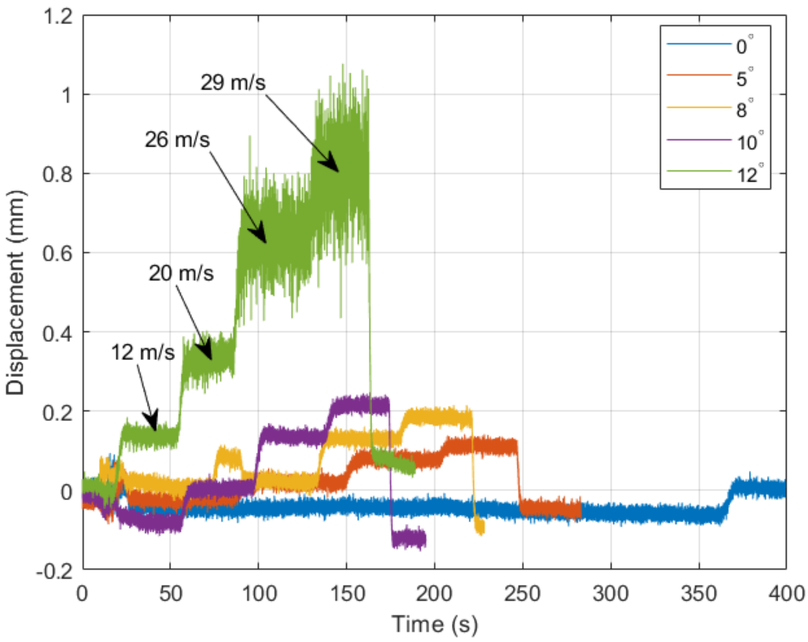

Figure 6: Gust vane trailing edge displacement at fixed displacement with increasing wind speed.

The data demonstrate the vanes are aeroelastically stable and exhibit only small displacement when under load. The desired gust amplitude in the initial experimental phase is below 5° of vane deflection. Within that range, the measured deflections are negligible. More work, by analysis and tests, on the deformation of gust vanes under loads and its effect is planned for the future.

Having cleared the system under static loads, work progressed to study gust vane system performance in the case of generation of dynamic discrete gusts.

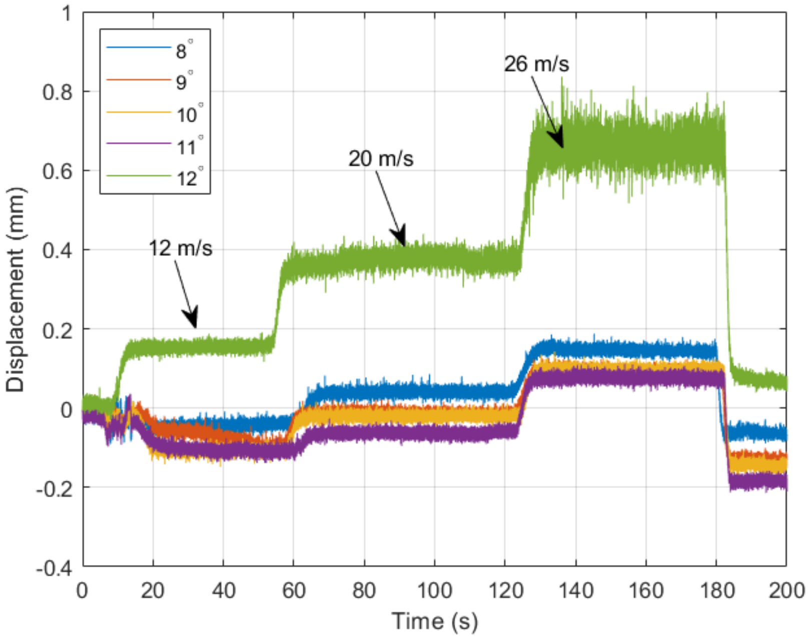

Figure 7: Measurements from follow-on static displacement tests.

3.2 Gust Response of the Aeroelastic Wind Tunnel Model

The gust vane control interface mentioned above currently constrains the types of disturbances that can be generated in the wind tunnel. The interface allows for input of gust amplitude (in degree of rotation of the gust vanes) and gust frequency. These parameters are universal for all gust input modes. There are a total of three different gust input modes from which to select. The main mode is a single discrete wave in the form of a 1-cos gust, simulating one of the required gust shapes in FAA certification criteria (FAR-25, see also [29]). The second mode is an extension of the first mode and allows for repeated 1-cos waves executed in given intervals, where the time between the gusts can be set in the interface. The last mode is a continuous gust with a simple sine shape.

The first mode is the most relevant for experimental GLA, as it follows the certification requirements for discrete gusts. The trajectory for the discrete $(1 - \cos(\omega t))$ gust is shown in Figure 8 (a).

A typical open loop response to a $(1 - \cos(\omega t))$ gust, measured by the root strain gauge of the wing, is shown in Figure 8 (b). Correlation of such measurements with predictions by the aeroservoelastic math model is shown in Figure 9. The $(1 - \cos(\omega t))$ gusts can be tuned to produce maximum dynamic responses at different points on the airframe.

The GGS was tested in all modes of its operation. Shakedown of the complete gust generation / wind tunnel / aeroservoelastic test article / control system was completed successfully shortly

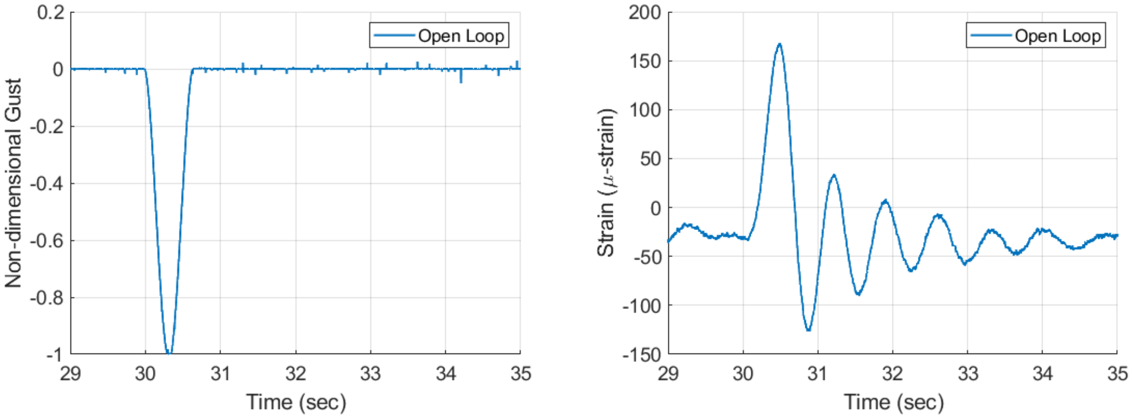

(a) Gust Profile

(b) Wing Strain

Figure 8: Open-loop gust system time histories.

thereafter. Only a few minor integration problems were encountered, and they were quickly solved. The development process of the GLA wind tunnel testing capability was overall very smooth.

4 GUST LOAD ALLEVIATION: CONTROL DESIGN AND RESULTS

The GGS was completed slightly after the wind tunnel test article and its systems became available. Therefore, initial tests were conducted using the test article's elevator as a disturbance source. This allowed for analysis of preliminary results and design feedback on the hardware setup and applied control techniques. Once the GGS was installed in the wind tunnel and the full system was verified in open-loop configuration, closed-loop tests could be set up and conducted, with experience from elevator disturbance tests supporting subsequent experiments.

The primary goal of these closed-loop tests was GLA of strains appearing in the wing due to the gust induced lift perturbation. In future work, uncertainty in the analytic plant model and robustness of the closed-loop system will be investigated. For the initial round of testing, verification and stability of the closed-loop system was the major concern. In the following section we will present the control methods applied in this first round of testing, show relevant results of the conducted experiments, and discuss the impact of these results and future plans for robustness tests. As a baseline, all experimental closed-loop results will be compared to the open-loop trajectories given in Figure 8 (b).

Model predictive control (MPC) was selected as the GLA method. This control technique allows for examination of disturbance preview information, inclusion of constraints, and optimal peak gust alleviation. It also follows the ongoing research effort at the University of Washington, where robustness of MPC is examined in varied ways. Practical robustness tests in the wind tunnel are among the experiments scheduled for future testing. Therefore, and in addition to stability and verification of the closed-loop, the following experiments were also designed to explore parameters and capabilities specific for online optimal control. Along with the real-time optimization capabilities of the soft- and hardware loop, the other objectives for the experiments were gust rejection and simple control comparison.

A controller to be compared with MPC was selected to evaluate the closed-loop results. The selected method was a linear quadratic regulator (LQR). This control design method yields a

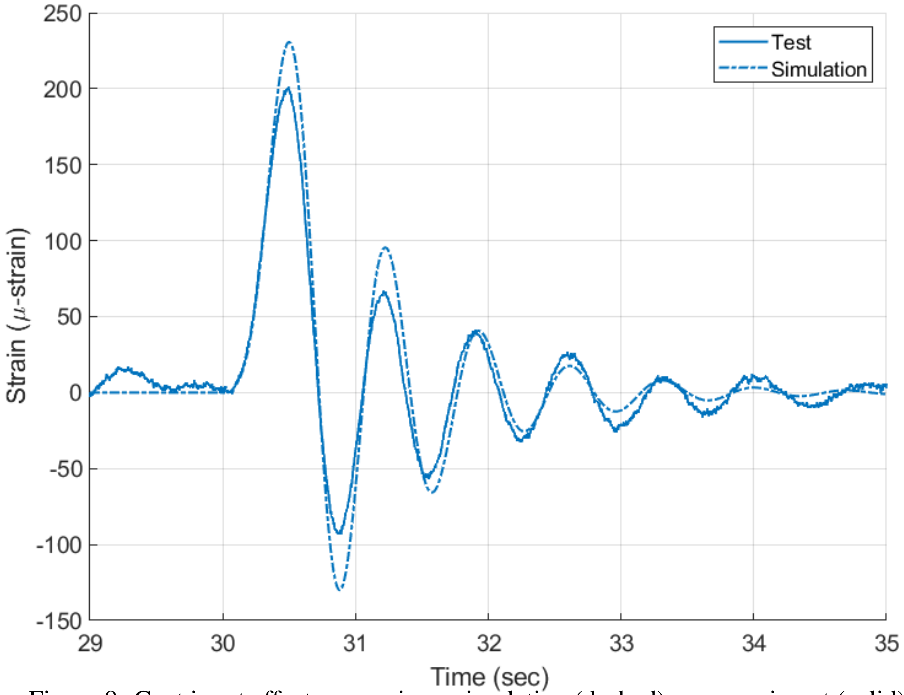

Figure 9: Gust input effect comparison, simulation (dashed) vs. experiment (solid).

full state feedback control law that is well suited for closed-loop system validation and optimal control comparison with MPC. With a linear model representation and a quadratic cost function, LQR forms a basis for evaluating MPC methods. First, a brief introduction for the LQR controller is presented. The theory behind the applied MPC system is given in the following subsection.

An LQR controller, as given in [30], is based on a linear plant representation. Being a state feedback method, only the state dynamics are required, see Eq. (1). Given these dynamics, the goal of an LQR controller is to minimize a quadratic cost function over an infinite time horizon. The optimal control problem can be formulated as:

$$\min_{u(t)} \int_0^\infty x(t)^\top Q x(t) + u(t)^\top R u(t)\, dt \tag{4}$$

with positive semi-definite state weight matrix $Q \in \mathbb{R}^{n\times n}$ and positive definite input weight matrix $R \in \mathbb{R}^{m\times m}$. The solution to this optimal control problem can be found via the Riccati equation and yields a negative state feedback control law:

$$u(t) = -Kx(t), \tag{5}$$

where K is the $m \times n$ feedback gain. As such, the LQR feedback gain depends on the plant matrices A and B, and the weight matrices Q and R. In the following, the reference to time t in the notation for time-varying signals will be omitted when appropriate.

For the application at hand, the weights need to be chosen to suppress gust loads by reducing wing-root bending moment. Usually, straightforward diagonal matrices with penalty weights for the respective state and control vector elements are preferable. With the dynamics given in Sec. 2, a general gust alleviation strategy should have increased weights on the first bending mode, η_1. The specific weights used for the initial testing phase are presented in the following discussion of MPC.

For both methods, a Kalman filter was used for state estimation. We reference [31] for more information on the basic, linear Kalman filter.

4.1 Model Predictive Control

The primary control method used for GLA in this work is MPC [32]. This method is an online optimization strategy. In general, it can be summarized as solving a given optimal control problem, usually with a finite time horizon, at the current time instance to generate an optimal control vector trajectory. The first entry of this trajectory is applied to the system as the control input. The whole procedure is then repeated at the next time instance. Due to this implementation of the optimal control trajectory, MPC is also called receding horizon control. Stability of MPC is and has been a major research focus in academia [33]. There are myriad iterations of this approach, with emphasis on different aspects of control theoretic properties, such as nonlinear dynamics, feedforward control, constrained states and inputs, and robust control.

The MPC strategy was selected due to its beneficial properties: optimal control for peak load alleviation; state and input constraints for requirement satisfaction; predictive capabilities for look-ahead disturbance measurement, such as LIDAR for gust preview. These properties are advantageous when dealing with aircraft dynamics in general and GLA specifically. Further research objectives in conjunction with the ongoing aeroservoelastic control project at the University of Washington is focused on robustness properties and analysis of MPC. The experimental results presented in this paper were aimed at preparing for the research on robustness, with tests having an emphasis on validation of real-time optimization and stability of the full closed-loop system, including software, hardware, and electronics setup.

The wind tunnel setup allows for closer examination of real-time application of MPC. Furthermore, using LQR as an additional test method, as mentioned above, allows for comparisons between two similar optimal control techniques. Using identical weights in the cost functions can help to highlight the improvements in performance when applying MPC.

4.1.1 Model Predictive Control Theory

The MPC method applied in the initial testing period follows a simple receding horizon control strategy. A detailed description and the theory behind the stability guarantees of this strategy can be found in [32]. Similar in its setup to LQR, linear MPC relies on linear model dynamics, see Eq. (1). As opposed to continuous time LQR though, linear MPC uses a discrete time description of the dynamics:

$$x(\tau + 1) = Ax(\tau) + Bu(\tau), \tag{6}$$

where A and B are the discretized dynamic matrices, $\tau = \frac{t}{\Delta t}$ is the discrete time parameter, given as an integer, $\tau = 0, 1, 2, \ldots$, and Δt is the discrete time interval in seconds. In addition to the control surface input in u, the MPC prediction dynamics include a disturbance preview input, u_d:

$$x(\tau + 1) = Ax(\tau) + Bu(\tau) + B_d u_d(\tau). \tag{7}$$

With this disturbance input, potential look-ahead measurements of the gust can be included in the prediction window of the MPC system. The disturbance preview, when included in the prediction horizon, has the potential to improve control performance considerably.

To solve the control problem and generate a control input for the plant, MPC attempts to find the minimum of a quadratic cost function. The cost function is given by:

$$\begin{aligned} V(x,u,\tau) &= \sum_{k=0}^{H_p-1} x_\tau(k+1)^\top Q x_\tau(k+1) + u_\tau(k)^\top R u_\tau(k), \\ \text{s.t.} \quad & x_\tau(k+1) = A x_\tau(k) + B u_\tau(k) + B_d u_d(\tau+k), \end{aligned} \tag{8}$$

where any parameter $a_\tau(\kappa) = a(\tau+\kappa)$, and H_p is the prediction horizon length given as a positive integer. The optimal control problem is to minimize this cost function with the inherent constraints of the discrete time dynamics. At each time instant, τ, the optimal cost, $V^*(\tau)$, and the optimal control trajectory

$$\mathbf{u}^*(\tau) = [u^*_\tau(0)^\top, \, u^*_\tau(1)^\top, \, \ldots, \, u^*_\tau(H_p-1)^\top]^\top \tag{9}$$

are determined. The control law reduces to the application of the first element, $u^*_\tau(0)$, to the plant as a constant control input. At the next time step $\tau+1$, the optimal control problem is solved again with the new state estimate and the whole procedure is repeated.

State or control constraints can be added to the optimal control problem as well, which will then still be readily solvable due to the finite time horizon. In the applications presented in this paper, constraints were not included.

4.1.2 Implementation

To run the MPC method in real time, it was written as a function in a Matlab script and then included in the real time environment loop of the Simulink model. The quadratic program (QP) was restructured and split into an offline element, the constant quadratic cost, and an online element, the state dependent vector. Matlab offers an online QP solver that has Simulink support and accepts these two elements as inputs to solve a QP.

The discrete state space dynamics in Eq. (7) can be written in extended matrix form as:

$$\mathbf{x}^+ = \mathbf{A}\hat{x} + \mathbf{B}\mathbf{u} + \mathbf{B}_d\mathbf{u}_d, \tag{10}$$

where bold vectors $\mathbf{x}$, $\mathbf{u}$, and $\mathbf{u}_d$ are vertically stacked vectors of the prediction window variables, and $\hat{x}$ represents the current state estimate, which is constant for the given prediction horizon. This notation reduces the dependence of the state prediction trajectory to the current state measurement and the optimization variable $\mathbf{u}$. The stacked matrices $\mathbf{A}$ and $\mathbf{B}$ are given by the original state matrices as follows:

$$\mathbf{A} = \begin{bmatrix} A \\ A^2 \\ \vdots \\ A^{H_p-1} \end{bmatrix}, \quad \mathbf{B} = \begin{bmatrix} B & 0 & 0 & 0 \\ AB & B & 0 & 0 \\ \vdots & & \ddots & 0 \\ A^{H_p-2}B & A^{H_p-3}B & \cdots & B \end{bmatrix}, \tag{11}$$

and $\mathbf{B_d}$ has a similar structure to $\mathbf{B}$.

The dynamics can be included inherently in the cost function of the optimal control problem in Eq. (8), removing the need for a sum and resulting in the structured cost given as:

$$V(\mathbf{x},\mathbf{u},\tau) = \mathbf{x}^\top\mathbf{Q}\mathbf{x} + \mathbf{u}^\top\mathbf{R}\mathbf{u}, \tag{12}$$

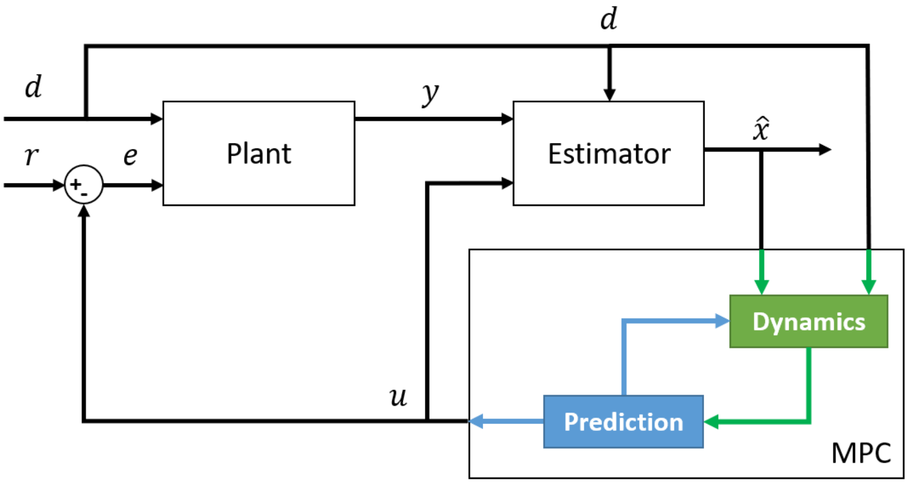

Figure 10: Block diagram for the Model Predictive Control implementation.

where matrices $\mathbf{Q}$ and $\mathbf{R}$ are block-diagonal, with the weighting matrices as repeated diagonal entries. When Eq. (10) is applied to the structured optimal control problem, the dependence on state information reduces to the current state estimate $\hat{x}_\tau$ at time τ and the problem has a single optimization variable in $\mathbf{u}$:

$$V(\mathbf{u}, \hat{x}_\tau) = \mathbf{u}^\top H \mathbf{u} + c(\hat{x}_\tau)^\top \mathbf{u}, \tag{13}$$

where H and c are optimization matrix and vector, respectively, which depend on the state and weight matrices described above. The optimal control problem with dynamical equality constraints has been reduced to a quadratic program.

Within Simulink the QP solver is integrated with a Matlab function block, taking the current state estimate, disturbance information, and prior solver parameters as inputs, returning the next control vector input and current solver parameters. For error-free execution of the MPC method, the solver has to find the optimal solution and return the next control input within the time frame defined by the chosen discrete time interval Δt. The implementation of the MPC system in block diagram form is shown in Figure 10.

For the initial GLA tests the relevant MPC parameters, such as time step size and prediction horizon, and the general weighting matrices for both LQR and MPC were designed based on prior simulation result. The selected values are given in Table 2.

Parameter	Value
Time Step Size	0.04 sec
Prediction Horizon	1 sec

(a) Prediction Parameters

Weights	Value
Angle of Attack	0
Pitch Rate	0.1
First Wing Bending	1
First Wing Bending Velocity	0.01
Actuators (IB & OB)	1

(b) Penalty Parameters

Table 2: Optimal Control Problem Parameters.

The cost function for the quadratic problem is implemented in Simulink by calculating the constant optimization matrix, H, and its inverse during the initialization of the simulation. During execution of the simulation, the optimization vector, c, is assembled based on given dynamics and weight matrices and the current state estimate. Both optimization paramters are then

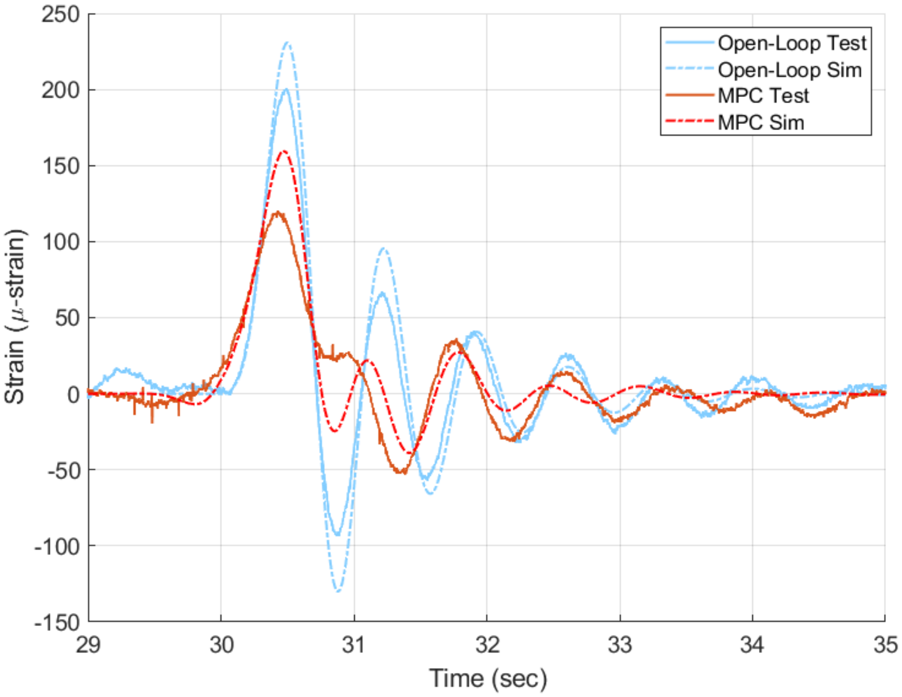

Figure 11: Open- and closed-loop result comparison of experiment (solid) and simulation (dashed) with a discrete gust disturbance.

fed into a built in quadratic programming solver. The solver is embedded in a custom Matlab function, which returns the next control signal to the plant.

4.2 Gust Load Alleviation Results

In closed-loop testing, both LQR and MPC control laws were applied to the system with identical weighting parameters. MPC had additional prediction parameters of a one second prediction horizon, 0.04 seconds time step size Δt, and gust preview information for the whole horizon. The experiments were conducted at a wind tunnel velocity of 20 $\frac{m}{s}$. The following section will discuss the results of the closed-loop experiments, comparing expectations from initial simulation runs to experimental measurements, and setting MPC side-by-side with the LQR controller to highlight some of the benefits achievable when employing MPC (at higher computational cost).

The primary control objective is to reduce the large initial peak in wing strain without adversely affecting other properties of the test article. In the following time histories, the gust occurs at 30 seconds.

A comparison between simulated and experimental active control of wing strain due to a gust is shown in Figure 11. The simulation (red) and the experiment (blue) match reasonably well in frequency. The wind tunnel data exhibit small variations in wing strain due turbulence in the flow and changes in environmental factors between test runs (i.e., temperature, small differences in tunnel setting). The key features of agreement are the timing of the peak gust and the rate of decay in the transient response. The larger magnitude response from the simulation is viewed favorably as conservative modeling error in terms of disturbance energy input to the system. The peak reduction in percent of the open-loop peak is higher in the experimental result. In simulation, the peak was reduced by 30.9%, from 230.5 to 159.4 μ-strain. During the

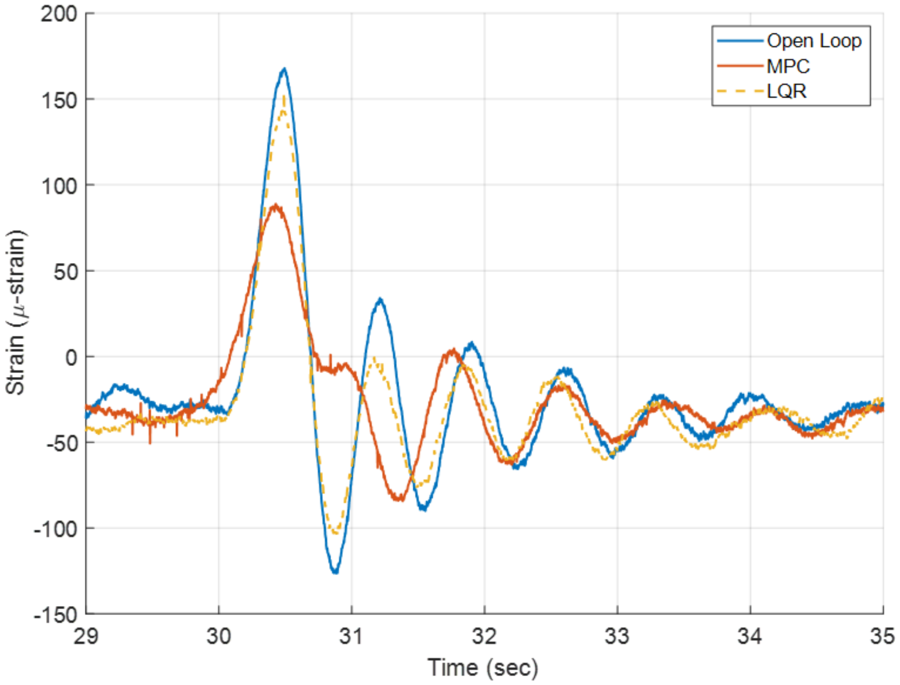

Figure 12: Closed-loop wing-root strain measurement.

experiment, MPC was able to reduce the peak load by 40.1%, from 201.1 to 120.4 μ-strain. This discrepancy can be an effect of the changing tunnel conditions. It could also result from model mismatch between the identified, linear simulation model of the plant and the actual, dynamic test article. Additionally, the Kalman filter performance may contribute to this difference. Future experiments, with more preparation and testing time for closed-loop settings, will revisit these results, checking for repeatability and model matching.

Closed-loop control comparison results are given in Figure 12 for the wing root strain measurement and in Figure 13 for the aileron inputs. Both figures include the MPC system as the main GLA method, with open-loop measurements as reference, and LQR results for closed-loop comparison. The open-loop response is shown in blue and the MPC response in red. LQR results are given in the dashed, yellow line.

Right away, it is visible that the MPC system reduces the peak load considerably. When looking at the peak values, the load is reduced by approximately 40%, as mentioned above. Furthermore, there is some shift in phase detectable right after the first peak. There is a plateauing between the first and second peak. This is where the effect of the control actuation, given in the aileron plot, is seen. The actuation towards the end of 31 seconds is very aggressive, especially in its derivative.

The residual response behaves similarly to the open loop, which could be explained by the plateau between the first and second peaks. This can be an indicator of the second peak being suppressed almost completely and a shift of the energy of that second peak into the remaining residual response. The visible discrepancy in the phase at about 31 seconds supports this point.

Comparing these results to the LQR case, we can see that LQR follows the open-loop trajectory more closely and acts almost as a pure damper. There is rather a small deviation from the open loop response and only towards the end of the residuals does the phase shift slightly from the

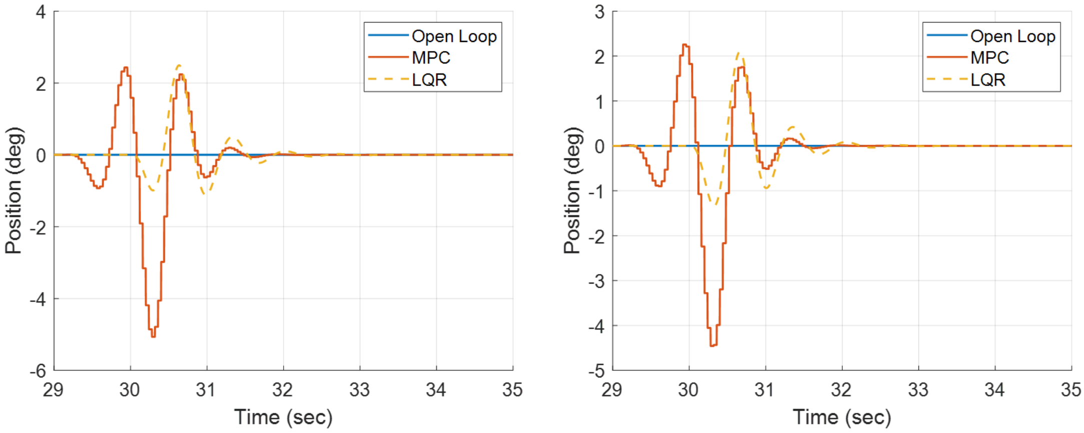

Figure 13: Closed-loop aileron deflection.

open-loop. In this case, the load alleviation is less than what is achieved in MPC, the peak load is reduced by approximately 12%. Both the lesser load reduction and the better matching trajectory shape can be explained by the utilization of the disturbance preview information and shorter horizon window for the MPC optimization.

The aileron deflection employed by both methods is presented in Figure 13. In this figure, the outboard aileron deflection is shown on the left panel, and the inboard aileron deflection is on the right. For both controllers, the input trajectories are similar for both ailerons, with the outboard aileron utilized slightly more. Of note is the earlier initial actuation of MPC. In this case, the controller reacts to the disturbance preview information and deflects the ailerons about a second before the gust hits at 30 seconds. Once the actuation begins, MPC uses much more deflection to deal with the peak load, as the dynamical prediction with preview information supports load alleviation. Once the test article experiences the gust, both LQR and MPC follow similar trajectories, with almost identical frequencies and peaks (30-32 seconds). With the head start inherent in MPC, the initial combined peak deflection is higher than that of LQR. Later peaks are then less in amplitude, as MPC has already successfully reduced the loads at this point in the trajectory.

5 CONCLUSION

New wind tunnel aeroservoelastic model design, construction, and testing capabilities at the University of Washington make it possible to efficiently evaluate the performance of different active control techniques for the suppression of gust responses on aeroservoelastic flight vehicle models of interest. The paper includes an overview of these new capabilities. In particular, an effective means for comparing the performance of established and new gust alleviation and stability augmentation control methods is provided. We believe that this effort provides very useful insights and lessons to the expanding field of active aeroservoelastic control of modern flexible flight vehicles.

Acknowledgement

The work reported in this paper has been supported by a research grant from the Boeing Company. The authors gratefully acknowledge their many discussions with Kioumars Najmabadi, Brian Rupnik, Gregory Clark, Alexander Ho, and Prachya Panyakeow at the Boeing Company.

6 REFERENCES

[1] Regan, C. D. and Jutte, C. V. (2012). Survey of applications of active control technology for gust alleviation and new challenges for lighter-weight aircraft.

[2] Livne, E. (2018). Aircraft active flutter suppression: State of the art and technology maturation needs. *Journal of Aircraft*, 55(1), 410–452.

[3] Ham, N. D., Bauer, P. H., and Lawrence, T. L. (1974). Wind tunnel generation of sinusoidal lateral and longitudinal gusts by circulation of twin parallel airfoils. *NASA Technical Report, NASA-CR-137547*.

[4] Redd, L. T., Hanson, P. W., and Wynne, E. C. (1979). Evaluation of a wind tunnel gust response technique including correlations with analytical and flight test results. *NASA Technical Paper*.

[5] Tang, D., Cizmas, P. G. A., and Dowell, E. H. (1996). Experiments and analysis for a gust generator in a wind tunnel. *Journal of Aircraft*, 33(1), 139–148.

[6] Cizmas, P. G. A., Tang, D., and Dowell, E. H. (1996). Flow about a slotted cylinder-airfoil combination in a wind tunnel. *Journal of Aircraft*, 33(4), 716–721.

[7] Xu, H., Xing, S., and Ye, Z. (2015). Numerical study of an airfoil/rotating-slotted-cylinder based flutter exciter. *Journal of Aircraft*, 52(6), 2100–2105.

[8] Tang, D. and Dowell, E. H. (2002). Experimental and theoretical study of gust response for high-aspect-ratio wing. *AIAA Journal*, 40(3), 419–429.

[9] Tang, D., Henry, J. K., and Dowell, E. H. (2000). Nonlinear aeroelastic response of delta wing to periodic gust. *Journal of Aircraft*, 37(1), 155–164.

[10] Poussot-Vassal, C., Demourant, F., Lepage, A., et al. (2017). Gust load alleviation: Identification, control, and wind tunnel testing of a 2-d aeroelastic airfoil. *IEEE Transactions on Control Systems Technology*, 25(5), 1736–1749.

[11] Babbar, Y., Suryakumar, V. S., and Strganac, T. W. (2013). Experiments in aeroelastic response and control under gust. *AIAA Paper*.

[12] Babbar, Y., Suryakumar, V. S., Strganac, T. W., et al. (2015). Measurement and modeling of aeroelastic response under gust. *AIAA Paper*.

[13] Harding, S. F., Payne, G. S., and Bryden, I. G. (2014). Generating controllable velocity fluctuations using twin oscillating hydrofoils: experimental validation. *Journal of Fluid Mechanics*, 750, 113–123.

[14] Neumann, J. and Mai, H. (2013). Gust response: Simulation of an aeroelastic experiment by a fluid?structure interaction method. *Journal of Fluids and Structures*, 38, 290–302.

[15] Wildschek, A., Maier, R., Hoffmann, F., et al. (2007). Wind tunnel testing of an adaptive control system for vibration suppression on aircraft. *AIAA Paper*.

[16] Lancelot, P. M. G. J., Sodja, J., Werter, N. P. M., et al. (2015). Design and testing of a low subsonic wind tunnel gust generator. *International Forum on Aeroelasticity and Structural Dynamics*.

[17] Mai, H., Neuman, J., and Hennings, H. (2011). Gust response: A validation experiment and preliminary numerical simulations. *International Forum on Aeroelasticity and Structural Dynamics*.

[18] Ricci, S. and Scotti, A. (2012). Wind tunnel testing of an active controlled wing under gust excitation. *AIAA Paper*.

[19] Fonte, F., Riccobene, L., Ricci, S., et al. (2016). Design, manufacturing and validation of a gust generator for wind tunnel test of a large scale aeroelastic model. *Congress of the International Council of the Aerospace Sciences*.

[20] Saddington, A. J., Finnis, M. V., and Knowles, K. (2015). The characterisation of a gust generator for aerodynamic testing. *Proc IMechE Part G: J Aerospace Engineering*.

[21] Bateman, D. (2017). *Design and Qualification of an Upstream Gust Generator in a Low-Speed Wind Tunnel*. Master's thesis, University of Colorado.

[22] Wood, K. T., Cheung, R. M., Richardson, T., et al. (2017). A new gust generator for low speed wind tunnel: Design and commissioning. *AIAA Paper*.

[23] Quenzer, J., Barzgaran, B., Mesbahi, M., et al. (2018). The generic wide body aircraft model. In *2018 AIAA Guidance, Navigation, and Control Conference*. American Institute of Aeronautics and Astronautics, p. 0877. doi:10.2514/6.2018-0877.

[24] Quenzer, J., Zongolowicz, A., Hinson, K. A., et al. (2019). Model for aeroelastic response to gust excitation. In *AIAA Scitech 2019 Forum*. p. 2031.

[25] Pankonien, A. M. and Reich, G. W. (2018). Multi-material printed wind-tunnel flutter model. *AIAA Journal*, 56(2), 445–457.

[26] Milne, R. D. (1964). Dynamics of the deformable aeroplane. Aeronautical research council reports and memoranda, University of London (Queen Mary College).

[27] McLean, D. (1990). *Automatic flight control systems*. Englewood Cliffs, NJ: Prentice Hall.

[28] Schmidt, D. (2012). *Modern flight dynamics*. McGraw-Hill Higher Education.

[29] (2015). Certification specifications and acceptable means of compliance for large aeroplanes cs-25.

[30] Skogestad, S. and Postlethwaite, I. (1996). *Multivariable Feedback Control*. Wiley.

[31] Crassidis, J. L. and Junkins, J. L. (2012). *Optimal Estimation of Dynamic Systems*. CRC Press.

[32] Rawlings, J. B. and Mayne, D. Q. (2009). *Model Predictive Control: Theory and Design*. Nob Hill Publishing.

[33] Mayne, D. Q., Rawlings, J. B., Rao, C. V., et al. (2000). Constrained model predictive control: Stability and optimality. *Automatica*, 36(6), 789–814.